Bulgarian Chemical Communications, Volume 55, Special Issue A (pp. 5-11) 2023 *DOI: 10.34049/bcc.55.A.0001*

Effect of calcination on nickel-doped calcium hydroxide nanoparticles

Akash[1], R. Singhal[2], M. G. H. Zaidi[3], S. Rawal[4], A. K. Mukhopadhyay[4], P. Kumar[1*]

[1]Department of Physics, Manipal University Jaipur, Jaipur-303007, Rajasthan, India
[2]Department of Physics, Malaviya National Institute of Technology, Jaipur-302017, India
[3]Department of Chemistry, College of Basic Science and Humanities, G.B Pant University of Agriculture and Technology, Uttarakhand, 263145, India
[4]Department of Physics, Sharda School of Basic Sciences and Research, Sharda University, Greater Noida 201310, Uttar Pradesh, India

Received: March 15, 2023; Revised: April 24, 2023

In this study, we have synthesized calcium hydroxide (CH) and nickel (Ni)-doped calcium hydroxide nanoparticles (NPs), through the inexpensive chemical precipitation route. The nickel-doped CHNPs were then calcined at 500 °C for 3 hours. The produced samples were characterized by X-ray diffraction (XRD), scanning electron microscopy (SEM), energy dispersive X-ray (EDX), Fourier transform infrared spectroscopy (FTIR), and UV-visible spectroscopy techniques to investigate the changes in structural, morphological and optical parameters. The XRD study showed the phase formation of $Ca(OH)_2$, Ni-$Ca(OH)_2$, and $CaCO_3$. The $Ca(OH)_2$ nanoparticles were transformed into $CaCO_3$ NPs due to the high-temperature carbonation reaction. It was also found that the crystallite size is decreasing from 62.32 nm to 40 nm. The FESEM pictures expose the prepared samples' morphology and particle size. The UV-Vis spectra showed a blue shift in the absorbance band. The band gap energy of all prepared samples, plotted by Tauc's plot, showed a concomitant change with crystallite size.

Keywords: Calcium hydroxide, Calcium carbonate, Doping, Chemical synthesis.

INTRODUCTION

Due to its many commercial uses, calcium hydroxide ($Ca(OH)_2$), a semiconductor with a wide band gap [1], has become one of the most promising hydroxide materials in the fields of food packaging [2], wastewater treatment [3], and construction [4]. The material has many uses in different categories, which involve dental cement [5], energy storage [6], cultural heritage conservation [7], antimicrobial activity [8], dye removal [9], and Portland cement production [10]. It is a fascinating semiconductor material because of its eco-friendliness and low cost when compared to other nanohydroxide materials. Nature makes it inevitable for humans to use materials in their daily lives, and there is a constant need for novel materials for a variety of uses, including solar cells, energy storage devices, magnetic materials, biosensors, dye degradation effects, and other applications [11]. As a result, for the preparation of nanostructured powders with a variety of compositions, sizes, and morphologies, improvements in powder processing procedures are required. For this instant, various categories of nanoparticles can be utilized to synthesize new materials. Due to their potential qualities and uses in optoelectronics, electronics, sensing, medicine, and catalysis, transition metals like Ni, Co, and Fe are of particular interest among the several categories of nanoparticles (NPs) [12, 13].

Recent studies have shown that after doping of such transition metals like Ni in ZnO nanoparticles the optical, structural, and morphological properties can be controlled and demonstrated effective biosensor applications and promising outcomes in the medical field [14]. Magnesium oxide and co-existing cobalt oxide agents have attracted considerable interest as the manufactured products retain an enormous surface area and band gap bowing. Thus, the obtained products may be crucial for photocatalysis [15]. Zinc oxide doped with transition elements (Ni and Cu) created by the chemical co-precipitation method demonstrates a blue shift in peak wavelength from undoped ZnO to doped ZnO in the PL spectra and a shift from lower to higher wavelength in the UV-Vis spectra [16]. Because of the differing electronic shell structure and comparable size of Ni^{2+} (0.069 nm) and Zn^{2+} (0.074 nm), it is anticipated that the doping of nickel in ZnO will change its absorbance, photocatalytic, and other physical or chemical assets. Research on Ni-doped ZnO nanostructures using spray pyrolysis, precipitation, and sputtering has also been described [17, 18].

This paper first reports the synthesis of Ni-doped CHNPs using the inexpensive co-precipitation

---

* To whom all correspondence should be sent:
E-mail: pushpendra.kumar@jaipur.manipal.edu

method. Then, the Ni-doped $Ca(OH)_2$ was calcined for 3h at 500 °C in air. This research sought to understand how calcination affected nickel-doped $Ca(OH)_2$ nanoparticles. The change in structural, morphological, and optical features of the primed nanoparticles was examined by various characterization methods including XRD, FTIR, FESEM, and UV-VIS. In this research report, the outcomes that were achieved are thoroughly addressed.

EXPERIMENTAL

Materials

All the chemicals, containing sodium hydroxide (NaOH), calcium nitrate hexahydrate ($Ca(NO_3)_2.6H_2O$), and nickel nitrate hexahydrate ($Ni(NO_3)_2.6H_2O$), obtained from Merck (India), were used as received. All the samples were prepared using deionized water throughout the experiment.

Method

In this experiment, calcium hydroxide and Ni-doped calcium hydroxide samples were prepared using the co-precipitation route. To create calcium hydroxide (sample A), $Ca(NO_3)_2.6H_2O$ and NaOH solution were prepared in distilled water. The precipitator sodium hydroxide (0.6 M, 200 ml) was dropwise added into the solution of calcium nitrate hexahydrate (0.6 M, 200 ml) while utilizing magnetic stirring at 1200 rpm solution, at room temperature. Following the completion of the reaction, the white precipitate was filtered from the remaining $NaNO_3$ using Whatman 40 filter paper (GE Healthcare UK Limited, UK), that had been created during the synthesis. The white precipitate was dried at 60 °C for 2 hours. The synthesis of Ni-doped $Ca(OH)_2$ was also completed by the precipitation method. Firstly, (1-x) atom% $Ca(NO_3)_2.6H_2O$ and x atom% $Ni(NO_3)_2.6H_2O$ solution (where x = 0.10) were made in 200 ml distilled water. The calcium nitrate hexahydrate (0.6 M, 200 ml) solution was then mixed into nickel nitrate hexahydrate (0.6 M, 200 ml) on a magnetic stirrer under continuous mixing. In addition, NaOH aqueous solution (0.6 M, 200 ml) was made of deionized water and then mixed dropwise into the aforesaid solution while utilizing magnetic stirring at 1200 rpm. The entire process was held at normal temperature. Following an hour of applying the precipitator NaOH, the precipitate was acquired and filtered using Whatman 40 filter paper. The $NaNO_3$ residue was also removed by repeated washing with deionized water. Finally, the Ni-$Ca(OH)_2$ precipitate was dried at 60°C for 2 hours in the air. The final product was denoted as sample B. Finally, Ni-doped $Ca(OH)_2$ (sample B) was calcined at 500 °C for 3 hours in the air, and assigned as sample C.

Characterization techniques

An X-ray diffractometer (Rigaku Miniflex-II, Japan) was used to characterize the phases of the product samples. It used a diffractometer with wavelength Cu K_α = 0.15406 nm, an angle range of 10-80°, and a step size of 0.02°. The FESEM (JEOL JSM-7610FPlus) with an EDX spectrometer connected was used for the microstructural analysis and elemental composition. The functional group information of all the dry samples was gathered with an FTIR spectrometer (KBr, Bruker Alpha, USA). The data were recorded over the 500–4000 cm^{-1} wavenumber. (UV-vis) absorbance spectra were obtained on a UV-Vis spectrometer (Shimadzu UV–NIR 2600, Japan) over the wavelength range of 190–800 nm. Using Tauc's Fig., the optical band gap values were computed.

RESULTS AND DISCUSSION

Structural study

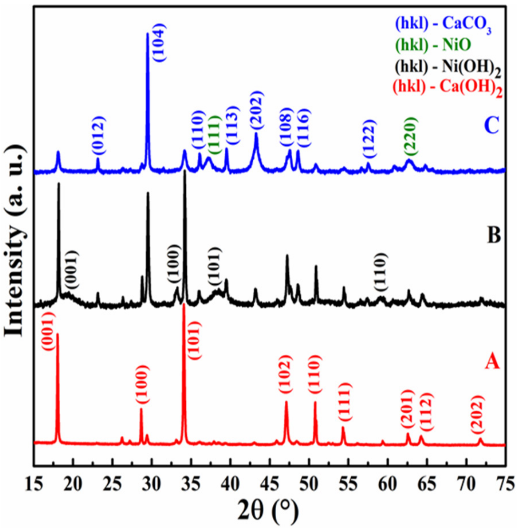

Fig. 1. X-ray diffraction pattern of samples A, B, and C.

The crystal structure of all prepared samples was studied by XRD analysis. In Fig. 1 (A-C), the XRD patterns of synthesized samples A, B, and C are shown. The $Ca(OH)_2$ phase seen in the XRD pattern shows typical diffraction peaks corresponding to (001), (100), (101), (102), (110), (111), (201), (112), and (202) appearing at 2θ values of, for instance, 18.04°, 28.67°, 34.09°, 47.12°, 50.80°, 54.35°, 62.60°, 64.26°, and 72.10° in turn. These data disclosed the hexagonal structure of calcium hydroxide nanoparticles with space group (P-3m1, No. 164) and had a good match with standard data, (PDF Card No. 00-004-0733) [19].

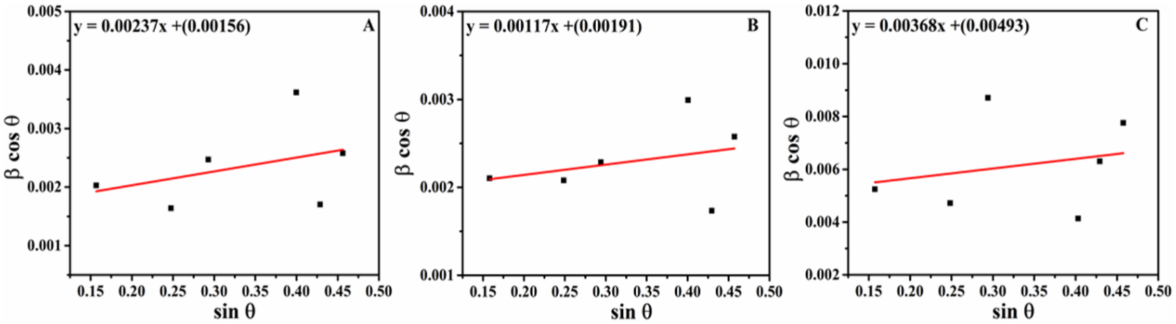

Fig. 2. Williamson–Hall plots of samples A, B, and C.

Furthermore, additional diffraction peaks corresponding to (001), (100), (101), and (110) on pattern B follow at the 2θ values of e.g., about 19.43°, 33.12°, 38.08°, and 59.13° in turn. It matches the published standard values with excellent precision (space group: P3m1, JCPDS card 742075) to the crystal phase of β-$Ni(OH)_2$ [20]. The XRD pattern shows the successful doping of the nickel atom into the CHNP structure. Numerous peaks conforming to the planes (012), (104), (110), (113), (202), (108), (116), and (122) appear respectively at 2θ values of, for instance, 23.11°, 29.44°, 36.12°, 39.54°, 43.30°, 47.50°, 48.61°, and 57.59° which are observed in the XRD pattern of sample C. The present pattern bouts with the standard rhombohedral calcite ($CaCO_3$) phase (space group No: 167, JCPDS card 00-005-0586) as the main phase and two minor peaks related to (111) and (220) at 2θ values of about 37.22° and 62.72°confirm the NiO phase [21, 22]. The calcite and NiO phases are induced due to the calcination process of nickel-doped calcium hydroxide nanoparticles. The result shows that the produced samples are polycrystalline in nature. Debye-Scherrer (D-S) formula is used to determine the average crystallite size using X-ray diffraction line broadening:

$$\delta = K\lambda / \beta\cos\theta \tag{1}$$

where δ stands for the crystallite size; K is the Scherrer constant valued to be 0.9; λ is the X-ray wavelength (Cu K_α, 1.54056 Å,); θ is the diffraction angle of the peak; and β is full-width at half-maxima (FWHM) (in radian) [23]. The crystallite size for samples A, B, and C is 62.32 nm, 56.75 nm, and 40.00 nm, respectively. The crystallite size as well as if the (D-S) methodology provides the correct trend of the nanocrystallite size data were confirmed using the Williamson-Hall method [24]. The equation below was used for the same:

$$\beta \cos\theta = \frac{k\lambda}{\delta_{W-H}} + 4\,\varepsilon \sin\theta \tag{2}$$

where β is the FWHM. Moreover, k has a constant value of ~0.9 [19]. Here λ denotes the wavelength, which is 1.506 Å. For samples A, B, and C, the quantity (cos) as a function of (sin) was then linearly fitted. The sizes of the crystallites (W-H) were estimated for each sample using the intercepts on the Y-axes of the linear interpolations of the corresponding fitted lines. The proper W-H plots for samples A, B, and C are depicted in Figs. 2(a), (b), and (c), respectively. Using the equation below, the dislocation density (ρ_d) of the prepared samples was determined:

$$\rho_d = \frac{1}{\delta^2} \tag{3}$$

According to calculations, CH sample A has a dislocation density of~ (2.5×10^{14} m^{-2}). Whereas, for the Ni-CHNPs sample B it increased to ~ (3.1×10^{14} m^{-2}), and for $CaCO_3$ sample C the value also increased to ~ (6.2×10^{14} m^{-2}). A smaller crystallite size suggests a greater surface-to-volume ratio. The dislocation network in the smaller crystallites is prevalent with a higher surface-to-volume ratio. So, more dislocations per unit area are raised in this case, accommodating the reduced crystallite size [25]. Table 1 summarizes the crystallite size with both δ_{D-S}; and δ_{W-H} data with the dislocation density and band gap energy. The prepared samples A, B, and C have crystallite sizes in the following order: A > B > C, for both δ_{D-S}; and δ_{W-H} values. The crystallite size is decreasing because the dopant ion will substitute itself into the structure of $Ca(OH)_2$ as the dopant's ionic radius is smaller than that of the host material; if the ionic radius is bigger, the ions will be embedded *via* an interstitial process. The interstitial process causes a disruption in the structure, resulting in a positive charge around the crystal or the formation of an oxygen vacancy [26]. Since the ionic radius of Ni^{2+} (83 pm) is smaller than that of Ca^{2+} (114 pm), the drop in crystallite size is most likely the result of the deformation process caused by Ni atom replacement into the CHNP structure. The main root cause of the decrease in crystallite size was the distortion of the host lattice of $Ca(OH)_2$ caused by the hosted ions Ni^{2+}, which decreased nucleation and slowed the growth of $Ca(OH)_2$ nanoparticles.

Table 1. Crystallite size, dislocation density, and bandgap of samples A, B, and C.

Sample	Crystallite size, $\delta_{D\text{-}S}$ (nm)	Crystallite size, $\delta_{W\text{-}H}$ (nm)	Dislocation density, ρ_d (m^{-2})	Bandgap (eV)
A	62.32	88.88	$2.5 * 10^{14}$	4.83
B	56.75	72.59	$3.1 * 10^{14}$	5.55
C	40.00	28.12	$6.2 * 10^{14}$	5.64

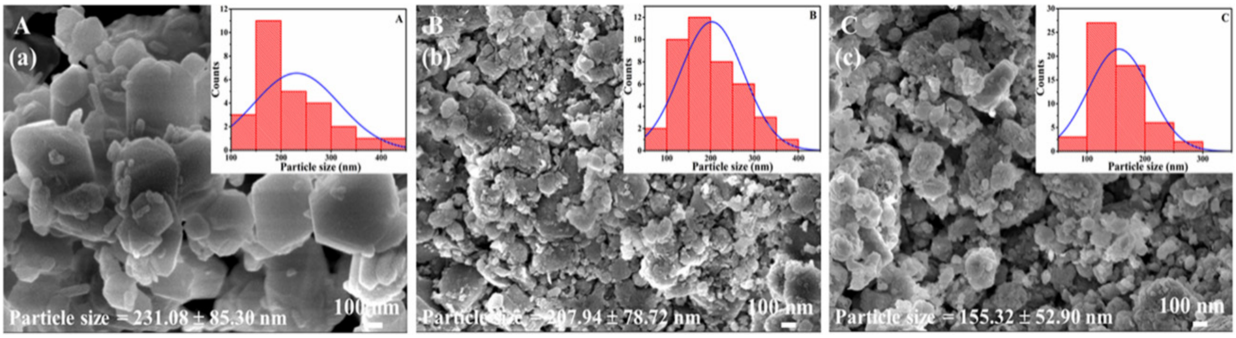

Fig. 3. FESEM photomicrographs of samples A, B, and C.

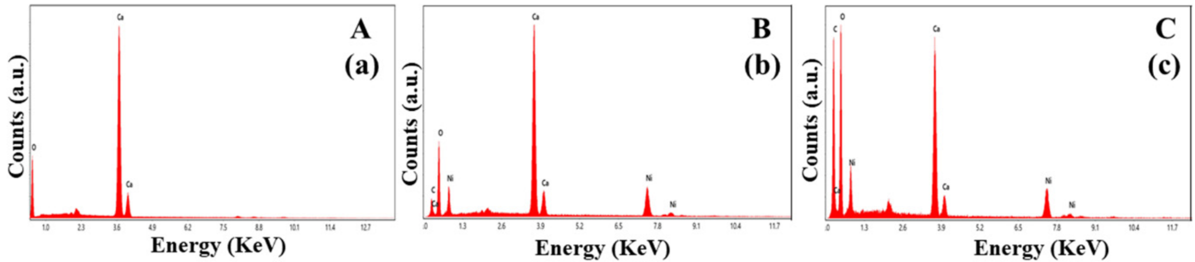

Fig. 4. EDX spectra of samples A, B, and C.

After the calcination, particle size generally increases due to aggregation. But if the annealing temperature is improper (higher than the crystallization temperature or close to the melting point) then the material bonds will be disrupted, the order through the focused material will be increased and the crystallite size will consequently decrease.

FESEM study

The morphological study of the prepared samples A, B, and C was done by FESEM analysis. Fig. 3 shows the FESEM photomicrograph along with the corresponding EDX spectra of the prepared samples. From the study, the calcium hydroxide NPs (sample A) form nearly hexagonal-like structures (Fig. 3(a)) with a good contrast whereas the Ni-doped CHNPs and $CaCO_3$ have an irregular shape (Fig. 3(b), 3(c)) with more agglomerated particles. When related to calcium hydroxide sample A, the particles in both samples B and C have uneven size and shape.

The aggregation happens due to the highly active surface of the nanocrystallite. The average agglomerate size was 231.08 nm (Fig. *3*a*),* 207.94 nm (Fig. 3b), and 155.32 nm (Fig. 3c) for samples A, B, and C, respectively. The average agglomerate size was decreasing with the crystallite size. The insets of the corresponding FESEM pictures display the histograms for the distribution of agglomeration size. Fig. 4 displays the EDX spectra of all the generated samples. The EDX spectra of sample A approve the existence of Ca and O in CHNPs, which confirms the creation of calcium hydroxide as a main phase. Furthermore, the EDX spectrum of sample B is exposed in Fig. 4(b), confirming the considerable presence of Ni in addition to Ca and O. The presence of Ni validates the nickel doping in calcium hydroxide NPs, which matches XRD data well. Similar to this, in Fig. 4 (c), the EDX spectrum shows that sample C also contains a major amount of carbon in addition to Ca, O, and Ni. The occurrence of carbon in the EDX spectra supports the creation of the calcite phase. All the findings agree well with the XRD data.

FTIR study

The FTIR spectra of all prepared samples A, B, and C are presented in Fig. 5.

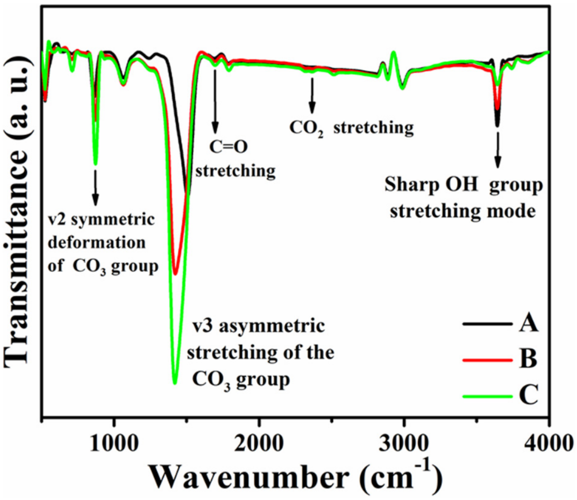

Fig. 5. FTIR spectra of samples A, B, and C.

The information was collected over a wavenumber range from 500 to 4000 cm^{-1}. The data has a good match with earlier published data [19, 21, 23]. FTIR shows an absorption band near ~ 3642 cm^{-1}, which is credited to the existence of the stretching mode of –OH groups in all samples. The absorption band of –OH groups is lowest in sample C, which can be due to the calcination of sample B at a high temperature. The large absorption band near ~1511 cm^{-1} in sample A is attributed to the v3 asymmetric stretching of CO_3 groups, which is shifted to the lower absorption band near ~1421 cm^{-1} in sample B. This change can be due to the nickel doping in CHNPs. Furthermore, a broad and intense peak at ~1421 cm^{-1} indicated the calcite phase in sample C. The C=O stretching mode was also thought to be responsible for the modest absorption bands that were found at around 2400 cm^{-1} in the ranges of every sample. All prepared samples exhibit the v2 symmetric distortion of the CO_3 group peak at the wave number of 860 cm^{-1}. The change in v2 symmetric distortion of the CO_3 group peak can also be seen in both samples B and C. As a result, these data also support the findings of the XRD studies.

UV-Vis spectroscopic analysis

The UV-Vis absorbance spectra were used to examine the optical characteristics of the prepared samples. The UV-Vis spectrum is presented in Fig. 6 as a function of wavelength.

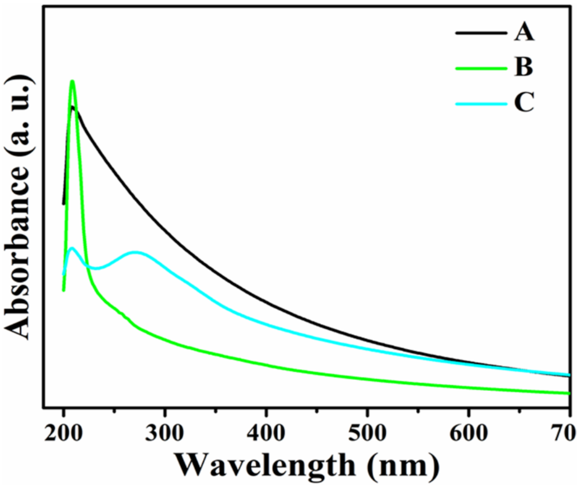

Fig. 6. Absorbance spectra of samples A, B, and C.

The sample absorbance can be affected by the band gap, surface roughness, impurity centers, and the quantum confinement effect [27, 28]. For CHNPs, Ni-CHNPs, and $CaCO_3$ NPs, the absorbance peaks originate at 256 nm, 223, and 219 nm, revealing a blue shift in absorbance. The band gap energy of the prepared samples was estimated by Tauc's plot as given below [29].

$$\alpha h\upsilon = A(h\upsilon - Eg)^{\frac{1}{2}} \tag{4}$$

where n (=1/2 for a direct band gap) is a constant, α is the optical absorption coefficient. The straight portion of the curve between "hυ" and $(\alpha h\upsilon)^2$ was extrapolated to determine band gap energy. Samples A, B, and C have band gap values of 4.83, 5.55, and 5.64 eV in order. Tauc's plot for the energy band gap is shown in Fig. 7. Hence, the optical band gap generally increases with the decrease in nanocrystallite size (Fig. 8), as expected.

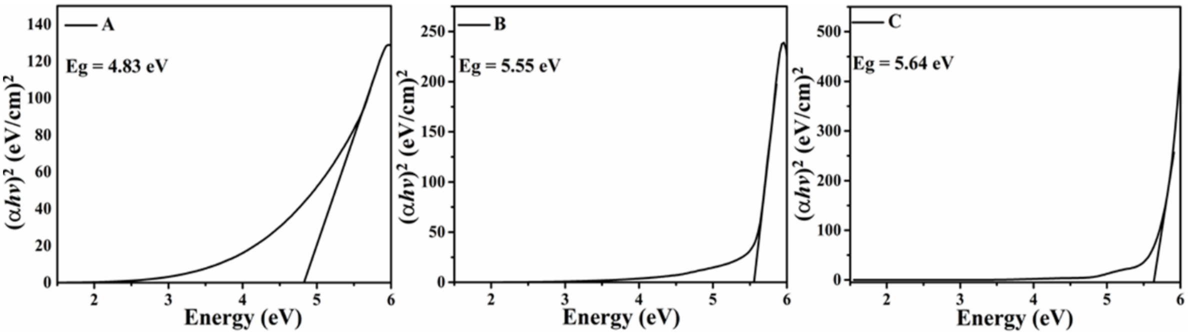

Fig. 7. Tauc's plots of samples A, B, and C.

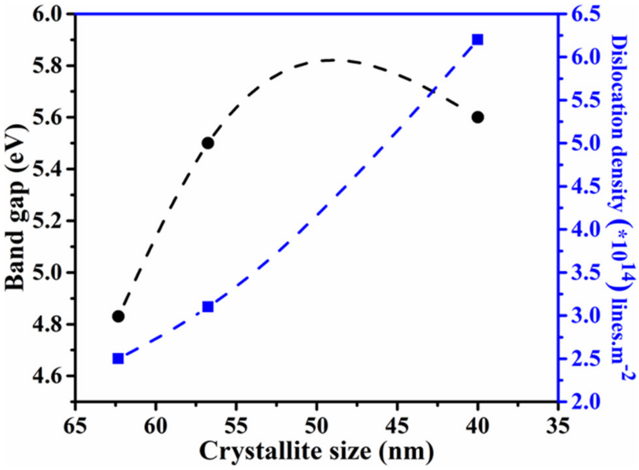

Fig. 8. Alteration in band gap and dislocation density with respect to crystallite sizes.

In general, the band gap energies could differ depending on the size of the nanoparticles. Since the ionic radius of Ni^{2+} (83 pm) is smaller than that of Ca^{2+} (114 pm), it was feasible for doping transition ions to occur, which resulted in a decreased lattice size in the samples. These findings indicate that Ni^{2+} transition metal ions have been successfully integrated into $Ca(OH)_2$ nanoparticles by replacing Ca^{2+} sites in the lattice. Additionally, when the average crystallite size decreased, the nanoparticles in use had higher band gap energies. The samples' smaller particle sizes caused the restricted dimension to shrink.

Further, the Fermi level in nominally doped semiconductors is situated between the conduction band and valence band. For the degenerate doping in semiconductors, the Burstein-Moss shift occurs because the conduction band edge density of states is exceeded by the electron carrier concentration. As the doping level is increased in n-type semiconductors, conduction band states are populated by electrons, increasing the energy of the Fermi level. The Fermi level of a degenerate level of doping is located inside the conduction band. Transmission/reflection spectroscopy is a tool that can be used to measure the actual band gap of a semiconductor. In a degenerate semiconductor, all the states below the Fermi level are occupied states, hence an electron from the top of the valence band can only be excited into the conduction band above the Fermi level (which is currently in the conduction band). In these occupied states, excitation is prohibited by Pauli's exclusion principle. Hence, we see a wider apparent bandgap [30].

CONCLUSION

In summary, calcium hydroxide and Ni-doped calcium hydroxide NPs were successfully produced through a precipitation process. The Ni-doped calcium hydroxide NPs were then calcined at 500°C temperature for three hours. The XRD data proved the phase formation of $Ca(OH)_2$, $Ni\text{-}Ca(OH)_2$, and that heating caused the calcite phase to develop. The nanocrystallite sizes of $Ca(OH)_2$, $Ni\text{-}Ca(OH)_2$, and $CaCO_3$ NPs were 62.32 nm, 56.75 nm, and 40.00 nm, in turn. The EDX data reinforced the existence of Ca, Ni, and C in the prepared NPs samples. The UV-Vis spectroscopy showed the energy band gap to be 4.83 eV, 5.55 eV, and 5.64 eV. The enhancement in the band gap may be attributed to the decrease in crystallite size.

Acknowledgment: *The corresponding author (Pushpendra Kumar) acknowledges the funding support from DST SERB with reference no. SUR/2022/004227 sanctioned on October 6, 2023, and the sophisticated analytical instrument facility (SAIF) and Central Analytical Facility (CAF) for the XRD, FESEM, FTIR, and UV-Vis spectroscopy measurements at Manipal University Jaipur. The first author, Akash, recognizes the scholarship (Sanction No. 09/1264(0005)/2020-EMR-I) he received from the CSIR.*

REFERENCES

1. A. Samanta, D. K. Chanda, P. S. Das, J. Ghosh, A. K. Mukhopadhyay, A. Dey, *J. Am. Ceram. Soc.,* **99** (3), 787 (2016).
2. H. G. Lee, C. H. Cho, H. Kim, S. R. Yoo, *Food Packag. Shelf Life*, **26,** 100558 (2020).
3. Harish, Pushpendra Kumar, A. G. Chakinala, R. Singhal, R. P. Joshi, A. K. Mukhopadhyay*, Chem. Select*, **7**, e202200393 (2022).
4. P. A. Basto, V. E. de Lima, A. A. de Melo Neto, *Constr. Build Mater.,***325**, 126767 (2022)
5. A. Zamanian, M. Yasaei, M. Ghaffari, M. Mozafari, *Ceram. Int.,***39**, 9525 (2013).
6. C. Huang, M. Xu, X. Huai, *Chem. Eng. Sci.,* **206,** 518 (2019).
7. V. E. García-Vera, A. J. Tenza-Abril, A. M. Solakb, M. Lanzón, *Appl. Surf. Sci.,***504,** 144195 (2020).

8. Harish, P. Kumar, S. Kumari, M. Debnath, A. Salim, R. Singhal, R. P. Joshi, A. K. Mukhopadhyay, *J. Mater. Sci.*, **57**, 8241(2022).
9. S. Pai, M. S. Kini, G. Rangasamy, R. Selvaraj, *Chemosphere,* **313**, 137476 (2023).
10. M. Kumar, S. K. Singh, N. P. Singh, *Thermochim. Acta*, **548,** 27 (2012).
11. G. Jayanthi, P. Kayalvizhi, *IJARIIT*, **7**(5), V7I5-1187 (2021).
12. E. I. Naik, H.S. B. Naik, M.S.Sarvajith, E. Pradeepa, *Inorg. Chem. Commun.***130**, 108678 (2021).
13. M. M. Obeid, S. J. Edrees, M. M. Shukur, *Superlattices Microstruct.* (2018), doi: 10.1016/j. spmi.2018.08.015
14. S. H.Basri, M. A. M.Sarjidan, W. H. Abd Majid, *Adv. Mat. Res.,***895,** 250 (2014).
15. M. M. Obeid, S. J. Edrees, M. M. Shukur, *Superlattices Microstruct.* (2018). doi: 10.1016/j. spmi.2018.08.015.
16. J. Chauhan, N. Shrivastav, A. Dugaya, D. Pandey, *J. Nanomed. Nanotechnol.,* **8**, 429 (2017).
17. K. Raja, P.S. Ramesh, D. Geetha, *Spectrochim. Acta,* **120**, 19 (2014).
18. N. Goswami, A. Sahai. *Mater. Res. Bull.,***48**, 346 (2013).
19. Akash, Harish, V. Kumar, R. K. Mishra, J. S. Gwag, R. Singhal, A. K. Mukhopadhyay, P. Kumar, *Luminescence*, **38**, 1297 (2023).
20. B. Shruthi, V. B. Raju, B. J. Madhu, *Spectrochim. Acta A Mol. Biomol*. Spectrosc., **135**, 683 (2015).
21. J. Kumari, Harish, Akash, A. Pandey, P. Kumar, M. K. Singh, A. Singh, M. S. Shishodia, R. P. Joshi, A. K. Mukhopadhyay, *Chemistry Select*, **7**(24), e202200416, (2022).
22. Z. Wei, H. Qiaoc, H. Yanga, C. Zhanga, X. Yan, *J. Alloys Compd.,* **479,** 855 (2009).
23. Akash, Harish, J. Kumari, A. K. Mukhopadhyay, P. Kumar, *Chem. Select*, **7**, e202200417 (2022).
24. Harish, P. Kumar, Akash, J. Kumari, L. Kumar, A. Salim, R. Singhal, A. K. Mukhopadhyay, R. P. Joshi, *Mater. Today Proc.,* **60**(1), 153 (2022).
25. A. Muiruri, M. Maringa, W. du Preez, *Mater.*, **13**(23), 5355 (2020).
26. D. Cahyaningsih, A. Taufik, R. Saleh, *J. Phys. Conf. Ser.,***1442,** 012017 (2020).
27. Harish, P. Kumar, V. Kumar, R. K. Mishra, J. S. Gwag, M. K. Singh, R. Singhal, and A. K. Mukhopadhyay, *Ceramic Int.*, **48**, 35771 (2022).
28. P. Kumar, P. Lemmens, *RSC Advance,* **5**, 91134 (2015).
29. Akash, Harish, V. S. Chouhan, R. Singhal, A. K. Mukhopadhyay, P. Kumar, *NanoWorld J.*, **8**(S1), S69 (2022).
30. C. Karthikeyan, L. Arun, A. S. Haja Hameed, K. Gopinath, L. Umaralikahan, G. Vijayaprasath, P. Malathi, *J. Mater. Sci. Mater. Electron,* **30**, 8097 (2019).